



Efficient, durable protection of the Ti6242S titanium alloy against high-temperature oxidation through MOCVD processed amorphous alumina coatings

Diane Samélor¹ , Loïc Baggetto¹ , Raphaël Laloo² , Viviane Turq² , Alain N. Gleizes¹ , Thomas Duguet¹ , Daniel Monceau¹ , and Constantin Vahlas^{1,*} 

¹ CIRIMAT - CNRS, Université de Toulouse, 4, Allée Emile Monso, BP-44362, 31030 Toulouse Cedex 4, France

² CIRIMAT - CNRS, Université de Toulouse, 118 Route de Narbonne, 31062 Toulouse Cedex 9, France

Received: 2 September 2019

Accepted: 6 December 2019

Published online:
12 December 2019

© Springer Science+Business
Media, LLC, part of Springer
Nature 2019

ABSTRACT

With their exceptional strength-to-weight ratio, titanium alloys find applications in numerous key enabling technologies. However, their implementation in harsh environments comes up against their limited resistance to high-temperature oxidation. To face this problem, in this work dense, amorphous alumina, Al₂O₃ coatings are applied on the surface of Ti6242S alloy by metalorganic chemical vapor deposition, MOCVD, from aluminum triisopropoxide, ATI and from dimethylaluminum isopropoxide, DMAI. Isothermal oxidation tests show that the parabolic rate constants of the mass gain of the coated Ti6242S coupons are reduced up to two orders of magnitude compared with the bare material. 5000 h long oxidation of DMAI Al₂O₃ coated alloy at 600 °C results in 0.180 mg cm⁻² weight gain to be compared with 1.143 mg cm⁻² for the bare alloy. In these conditions, an interfacial layer is formed, containing the complex Ti₃(Al_{0.5}Sn_{0.5}) (or (Ti,Sn)₂N) phase. Cyclic oxidation consisting of eighty, 1 h cycles between 50 and 600 °C show null mass gain of the coated sample. Finally, the hardness profiles determined on cross sections of oxidized coupons reveal a very limited oxygen dissolution for the coated alloy. MOCVD coatings of amorphous Al₂O₃ have great potential for efficient, durable protection against oxidation of Ti6242S alloys.

Introduction

With their exceptional strength-to-weight ratio, titanium alloys have been initially used in the aerospace (including advanced materials for jet engine) and defense sectors, and more recently in biomedicine

(including orthopedic or dental implants), recreational and other activities, or in the energy sector. However, their implementation in harsh environments comes up against their limited resistance to high-temperature oxidation. Such limited resistance is first due to the rapid formation of a very stable,

Address correspondence to E-mail: constantin.vahlas@ensiacet.fr

non-protective oxide layer, mainly composed of TiO_2 , on the surface of titanium alloys in contact with the air. More importantly, in these conditions a large amount of oxygen is inserted into the alpha hcp phase of Ti-alloys which can dissolve up to 33 at% O [1, 2]. The high concentration of O at the local equilibrium between the oxide and the metal results in a large diffusion flux of oxygen toward the bulk of the alloy. This diffusion generally affects a subsurface region that is much larger than the thickness of the external oxide layer. The properties of this subsurface volume drastically change in comparison with those of the bulk alloy. The cell parameter “c” of the hcp-Ti phase increases, the Young’s modulus and the hardness increase and the ductility decreases [3, 4]. These modifications result in the formation of surface cracks under tensile loading or thermal cycling [5]. To face this problem, several commercial, Ti-rich alloys, such as Ti–6Al–2Sn–4Zr–2Mo–0.1Si (wt%) (Ti–6242S), or Ti–5.8Al–4Sn–3.5Zr–0.5Mo–0.7Nb–0.35Si–0.06C (IMI 834) have been developed specifically for higher temperature use. They are much more resistant to oxidation than pure titanium [6, 7] but a thick, oxygen affected subsurface zone can still form at their upper temperature limit which does not exceed 500–600 °C. For example, a thickness of 40 μm is measured after only 500 h at 593 °C for the Ti6242S alloy [7]. In one step beyond, research is still active on the slight modification of the composition of these alloys with the aim to further improve their oxidation resistance [8].

In addition to the tuning of the alloy composition and microstructure, coating solutions have been investigated to both prevent oxygen ingress in titanium and Ti-alloys and limit the formation of the detrimental external oxide scale [9–14]. In this perspective, deposition of alumina, Al_2O_3 forming coatings have been successfully tested, mainly through the application of metallic Al films or powders, followed by a consolidative thermal treatment [10, 15–17]. However, the rough morphology of the source Al films diminishes the efficiency of the protective layer [18, 19]. Moreover, the reactive diffusion, which occurs at the superficial part of the alloy, results in the formation of an accidental zone composed of numerous oxide and/or intermetallic compounds, which is detrimental to the durability of the oxidation protection [10]. A more straightforward approach consists in the deposition of either pure Al_2O_3 [20–22] or Al_2O_3 containing glass coatings [14].

However, such coatings, often deposited through multistep wet processes, suffer high brittleness, which, combined with high film thickness (often largely exceeding 10 μm) result in spallation after limited service time [14].

We have shown that pure, amorphous Al_2O_3 thin films processed by metalorganic chemical vapor deposition (MOCVD) show promise for the efficient protection against high-temperature oxidation of titanium alloys [23, 24]. The present work subscribes to this approach by extending and completing recently published preliminary results [25]. It treats the question of the long-term efficiency of a rather thin barrier film. We apply by MOCVD amorphous Al_2O_3 films on a Ti6242S alloy and we submit the coupons to long-term isothermal oxidation experiments. We then investigate the microstructural and mechanical characteristics and we determine reaction kinetics. Finally, we illustrate the capacity of the amorphous Al_2O_3 coatings to sustain typical operating conditions of the titanium parts in aero turbines by cyclic oxidation tests at 600 °C.

Materials and methods

Thin film preparation and oxidation tests

Deposition of thin films was performed in a custom-made, horizontal, hot-wall reactor equipped with four gas lines and mass flow controllers (MFC), a large evaporation stainless steel chamber and a quartz tube (25 mm diameter, 300 mm length) heated by a resistive furnace. The setup is presented in details in [26, 27] The stainless steel sample holder is positioned in a uniform temperature zone at the center of the quartz tube. $10 \times 10 \times 1.6 \text{ mm}^3$ Ti6242S alloy (Ti–6Al–2Sn–4Zr–2Mo–0.1Si (wt%)) coupons are used as substrates. They are polished with 600 and 1200 grade SiC papers on both sides, and then, they are rinsed with water, acetone and ethanol and dried under argon flow. Gas lines and the evaporation steel chamber are heated to ca. 80 or 130 °C to prevent DMAI or ATI vapor condensation, respectively.

For deposition from ATI (98%, Acros Organics), the precursor is first melted above 140 °C and then maintained supercooled at 80 °C in a glass bubbler. During deposition, it is heated at 90 and 110 °C. 99.9999% pure N_2 (Messer) is used both as a carrier through the ATI bubbler and as a dilution gas. Fixed

experimental parameters are: total pressure 5 Torr, N₂ flow rate though ATI = 53 standard cubic centimeters per minute (sccm); dilution N₂ flow rate = 590 sccm. Deposition experiments are performed at 520 °C during 20 min resulting in 400-nm-thick amorphous Al₂O₃ films.

For deposition from DMAI, the precursor is injected to the deposition area with a direct liquid injection (DLI) technology, following a protocol described in details in [28]. The protocol consists in preparing a 0.2 M solution of DMAI (> 99%, Air Liquide) in anhydrous cyclohexane (99.5%, H₂O < 10 ppm, Sigma-Aldrich) without any contact with the air. For the 300 °C process, 120 sccm of N₂ bubbling through deionized H₂O (> 20MV cm) kept at room temperature is added to the reactor via another gas line. For the high-temperature (500, 700 °C) process, 50 sccm of O₂ (99.9995%, Air Products) is added to the N₂ dilution gas (300–400 sccm). In both cases, the oxidants are in large excess compared to DMAI.

The oxidation kinetics of uncoated and coated Ti6242S at different temperatures were determined in a single short run by using a high precision thermogravimetric apparatus equipped with a symmetrical furnace (SETARAM TAG 24 s). The protocol consists in increasing the temperature per stage while continuously measuring the mass gain of the sample. The results provide a first direct qualitative comparison between the systems. For cyclic oxidation tests, the same TGA apparatus was used. It allows thermal cycling with continuous recording of the mass [29]. The sensitivity of 0.1 µg allows for detection of tiny spallation events.

Materials characterization

Surface morphology and cross section of the samples were observed using two scanning electron microscopes (SEM). A FEI Helios 600i instrument composed of a field emission gun and a focus ion beam (FIB) operated between 5 and 10 kV was used for cross-sectional observations, electron dispersive spectroscopy (EDS) mapping and preparation of a thick slice (25 µm × 2 µm) for Auger mapping. A thin layer of platinum protected the samples. A FEI Quanta 450 (working in high, low, and environmental vacuum modes) operated at 10 kV was also used for cross section and surface morphology.

Crystallized phases were identified by X-ray diffraction (XRD) in low incidence (omega = 2°) with

a D8—BRUKER Advance instrument using a Cu Kα (1.5418 Å) X-ray tube operated at 40 kV and 40 mA, a Ni filter and a solid-state Lynxeye detector.

Surface element compositions were mapped by Scanning Auger microscopy (SAM) in a Thermo-electron MICROLAB 350 (Thermo Electron) analyzer. The surface was first submitted to Ar⁺ sputter (3 keV, 1.5 µA) cleaning. The mapping was recorded in snapshot mode with a primary e-beam of 10 keV and the built-in drift compensation.

For nanoindentation measurements, the cross-sectioned samples were mounted on an ultra-NanoIndenter apparatus from CSM Instrument (presently Anton Paar) fitted with a Berkovich diamond indenter. The loading–unloading sequence comprised gradual increase up to 30 mN in 30 s, stand-by for 15 s, then reversal down to zero in 30 s. Elastic modulus and hardness were extracted from the load versus depth curves with the method proposed by Oliver and Pharr [30]. Indents were positioned on a diagonal line through the cross-sectioned sample from the top surface to the diffusion zone and to the substrate (ca. every 7 µm). Measurements have been repeated 3 times: average values, as well as standard deviation are given in Fig. 9.

Results

Three samples were processed from dimethyl aluminum isopropoxide, DMAI at 300, 500 and 700 °C (DMAI300, DMAI500, and DMAI700, respectively). One sample was processed from aluminum triisopropoxide, ATI at 520 °C (ATI520). Figure 1 shows top view SEM micrographs taken in secondary electrons (SE) mode for ATI520 (Fig. 1a) and DMAI500 (Fig. 1b). Inserts show the corresponding cross sections, revealing that the deposited films have sub-micrometric thickness. The pristine alumina surfaces present nodules attributed to homogeneous, gas phase side-reactions producing powder particles that would incorporate with the growing film. The observed trenches correspond to the polishing patterns of the Ti6242S alloy coupons prior to deposition of Al₂O₃. The morphological characteristics of samples DMAI300 and DMAI700 are similar to those of sample DMAI500. From X-ray and electron diffraction, electron probe microanalysis, X-ray photoelectron spectroscopy and Rutherford backscattering spectroscopy, ATI300, DMAI300 and DMAI500 are

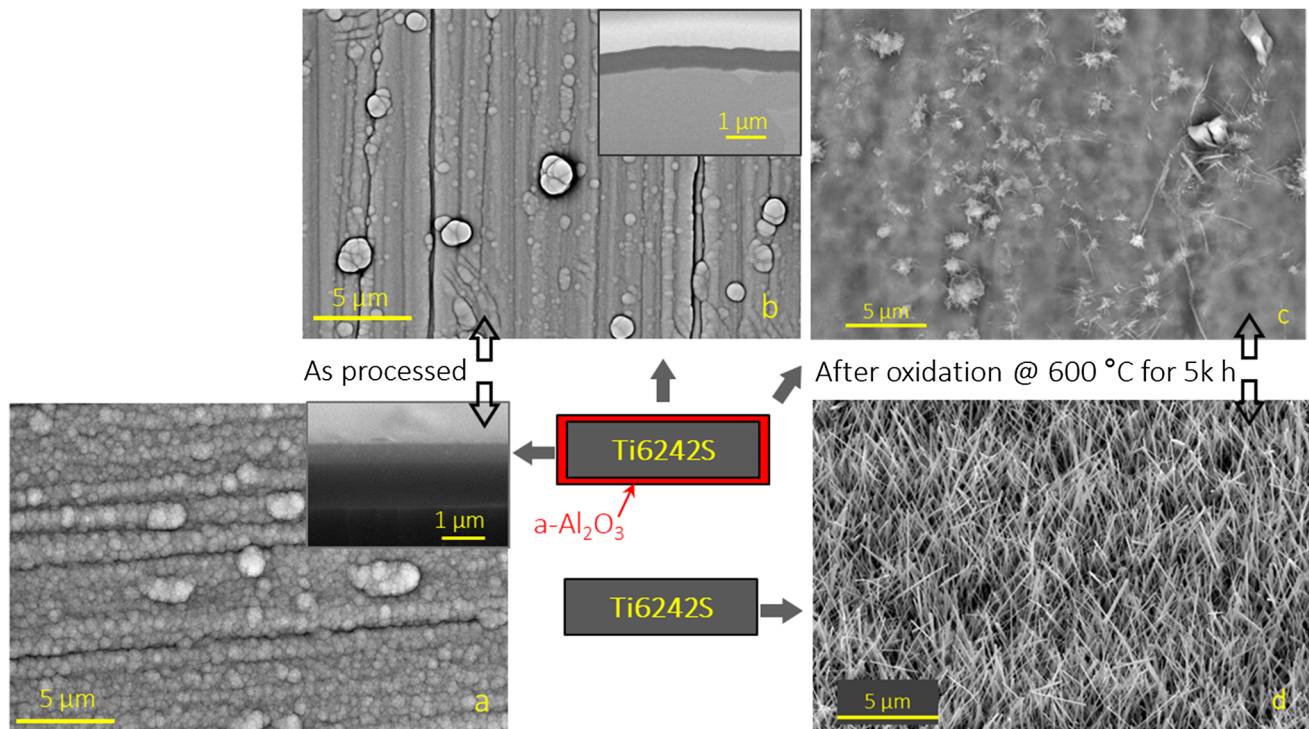


Figure 1 SEM secondary electrons surface micrographs of the as processed ATI520 (a) and DMAI500 (b) coatings on Ti6242S coupons as schematized in the center of the figure (not in scale).

made of stoichiometric, amorphous Al_2O_3 . When deposited from DMAI at 600 °C and above, like DMAI700, the aluminum oxide also contains carbidic carbon [28, 31, 32].

Figure 1 also presents surface SEM micrographs of two samples after 5000 h of isothermal oxidation at 600 °C. Micrograph 1d corresponds to the surface of bare Ti6242S. Thin, few-micrometers-long needles cover the entire surface. This morphology corresponds to the well-known acicular rutile that forms when bare Ti6242S oxidizes [33]. Micrograph 1c shows the surface of the DMAI500 sample. The amorphous Al_2O_3 surface has thinner and far less numerous needles than observed on the oxidized Ti6242S. In addition, we note the formation of a few excrescences. We will now focus on the microstructural characteristics of the DMAI500 samples after oxidation since, as it will be shown in next sections, Al_2O_3 films processed in these conditions present the best oxidation barrier properties and performance.

Figure 2 shows SEM images in backscattered electrons mode of cross sections obtained by FIB, and corresponding EDS maps of a bare Ti6242S alloy (Fig. 2a–e), a DMAI500 sample before (Fig. 2f–j) and

SEM-SE micrographs of two samples after 5000 h of isothermal oxidation at 600 °C: DMAI500 coupon (c) and bare Ti6242S (d).

after (Fig. 2k–o) oxidation at 600 °C during 5000 h. The bare Ti6242S cross section after oxidation (Fig. 2a) shows three layers. The top, 1.6 μm-thick layer corresponds to the needles observed in Fig. 1d, with a great density of large open pores. The intermediate, 2 μm-thick layer appears with a darker contrast and a high density of small pores. The deepest region corresponds to the semi-infinite part of the sample with the known microstructure of the alloy. The EDS mapping (Fig. 2b–d) reveals that a mixture of Ti and Al oxides have formed on the top layer of acicular rutile TiO_2 with a clear preferential segregation of Al from the bulk to the free surface. In contrast, the intermediate layer mainly contains Ti and O. Finally, Sn enrichment is observed at the $(\text{Ti}_2\text{O})/\text{Ti6242S}$ interface (Fig. 2e). This enrichment below the titanium oxide scale has been attributed to the selective oxidation of titanium and to the absence of dissolution of Sn in the scale, and to the fact that Sn oxide is not stable at the low oxygen pressure of the TiO_2/Ti interface.

We now focus on the SEM/EDX analysis of the as-deposited alumina/Ti6242S, and the oxidized film/substrate system. The as-deposited film is dense

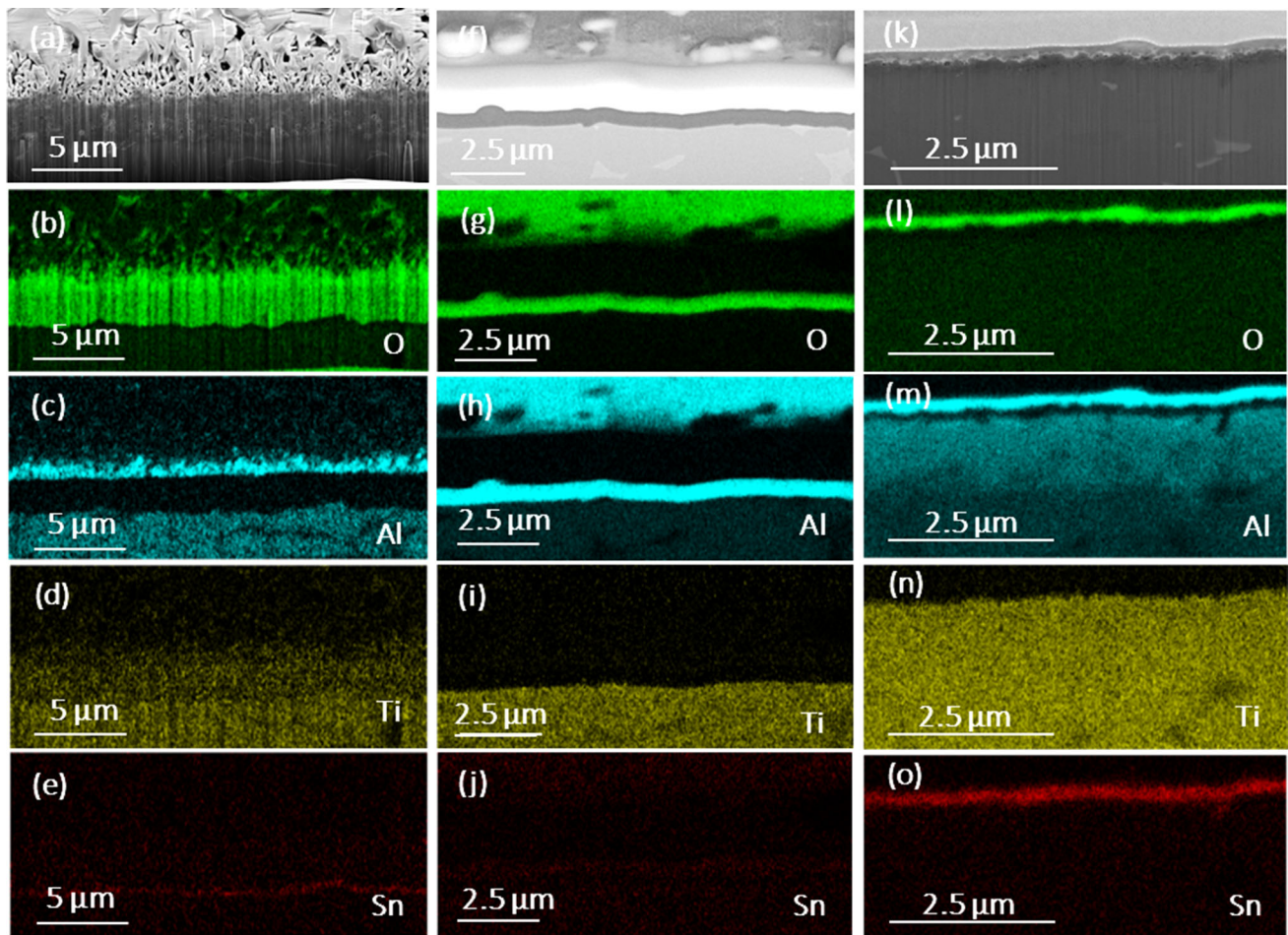


Figure 2 SEM cross sections of a bare Ti6242S after oxidation at 600 °C for 5000 h (a) and sample DMAI500 before (f), and after (k) oxidation at 600 °C for 5000 h. EDS mapping of O, Al, Ti and Sn elements after oxidation of a bare Ti6242S at 600 °C for

5000 h (b–e), of the as processed DMAI500 sample (g–j) and after oxidation of the DMAI500 sample at 600 °C for 5000 h (l–o).

(Fig. 2f), and EDS mappings (Fig. 2g–j) highlight sharp interfaces, with Al and O in the alumina layer, and Ti and some Sn within the alloy. Therefore, very little intermixing occurs during the CVD process at 500 °C. After thermal oxidation at 600 °C of a sample processed in the same conditions, the film/substrate assembly shows strong modifications in terms of microstructure and chemical composition. Figure 2k shows microstructural changes near the initial alumina/Ti6242S interface, where pores are now visible. In this porous region, a mixed Ti, O, Al layer has replaced the Al_2O_3 coating. At the end of the oxidation, the thickness of the initial alumina protective film has halved.

The thermodynamic stability of alumina on a titanium alloy can be lower than the stability of titanium oxide, when the Al activity in the alloy is low enough

[34]. Therefore, the alumina layer dissolves slowly in the titanium alloy releasing O and Al in the metal. This explains the decrease in the alumina layer thickness and the observed Al enrichment 1.3 μm deep in the alloy (Fig. 2m). It is well known that these two elements stabilize Ti- α but also Ti- α_2 (Ti_3Al) [3]. But, the cross section Fig. 2i–o also reveals an additional, 300 nm thick layer strongly enriched in Sn and depleted in Al. This metallic layer cannot be Ti- α , Ti- α_2 or Ti- β . Diffraction work is necessary to identify this Sn-rich layer formed during the interdiffusion of alumina with Ti6242S in air.

Figure 3 shows a SEM cross-sectional micrograph and scanning Auger microscopy (SAM) maps of the DMAI500 sample after oxidation. The large excrement visible in the image was deteriorated during oxidation, and it now presents large pores and low

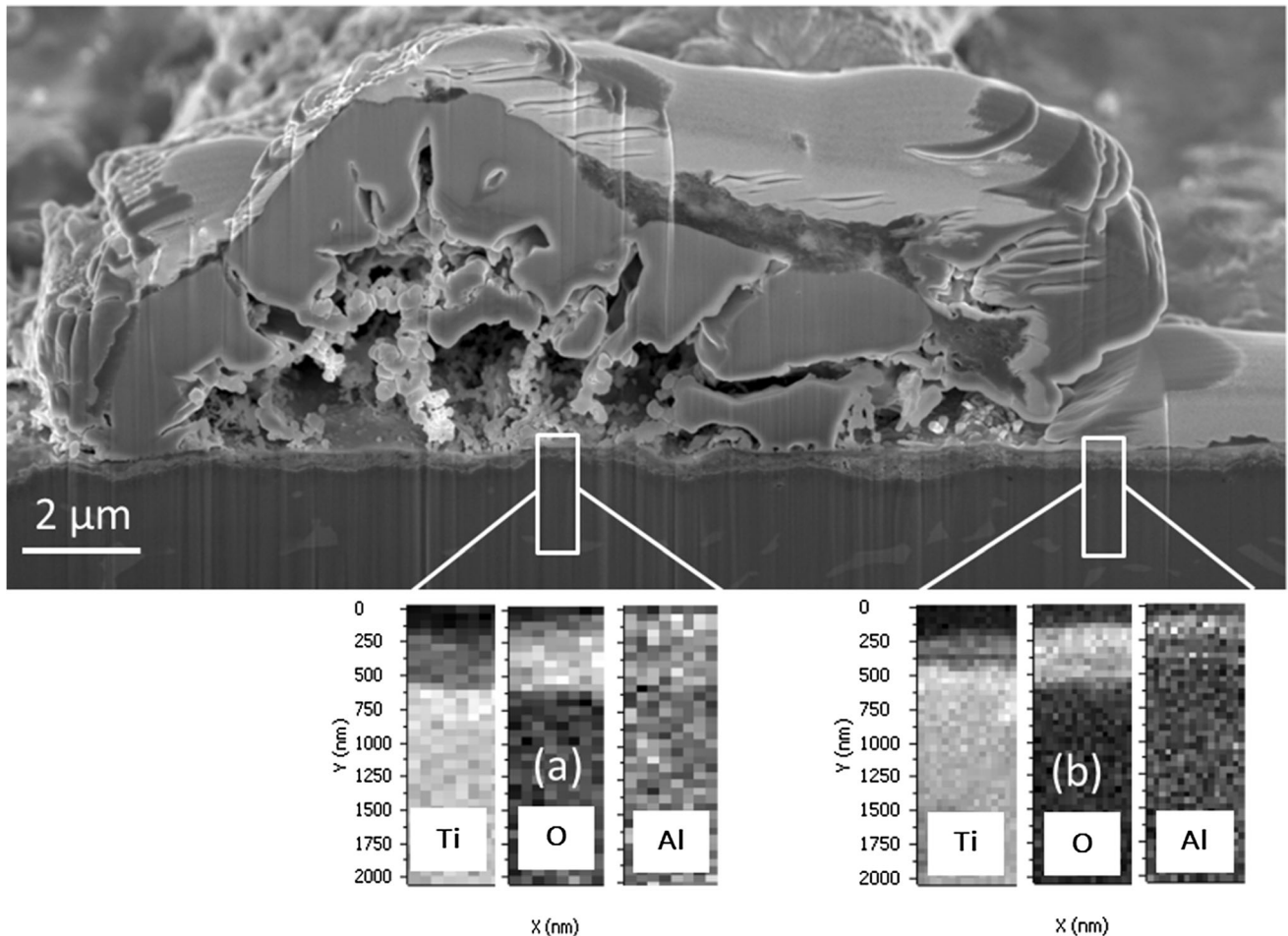


Figure 3 FIB-SEM cross section and Auger mapping of the DMAI500 sample after oxidation during 5000 h at 600 °C. **a** Area under an “excrecence”, **b** area without “excrecence”.

cohesion with the underlying coating/substrate. The two regions we investigate with SAM do not behave in the same way upon oxidation, depending on their position in relation to the excrecence. Underneath the excrecence, SAM map of Fig. 3a shows that the initial 500-nm-thick Al_2O_3 coating has been replaced by two layers: a 400 nm thick (Ti, Al, O) layer and a 100 nm thin (Al, O) layer. Apart from the excrecence, map Fig. 3b shows that the (Ti, Al, O) layer is thinner (approx. 250 nm after accounting for an experimental downward drift during acquisition), indicating that the excrecence could represent a preferred oxidation pathway. These observations suggest that the excrecence is a weakness for the barrier properties of the Al_2O_3 coating.

Figure 4 shows the low incidence ($\omega = 2^\circ$, and $\omega = 0.5^\circ$ in the insert), X-ray diffraction pattern for

DMAI500 after thermal oxidizing treatment at 600 °C for 5000 h. The diffraction lines of six phases have been identified: alpha-Ti, rutile TiO_2 , $\alpha\text{-Al}_2\text{O}_3$, a transition Al_2O_3 , TiN, and $\text{Ti}_3(\text{Al}_{0.5}\text{Sn}_{0.5})$. Al and Ti oxides give rather weak peaks. Raman spectroscopy confirms the presence of alpha- Al_2O_3 . Two peaks at $2\theta = 45.9^\circ$ and 67.0° clearly correspond to a transition alumina, but Raman spectroscopy did not allow identifying it in the presence of corundum. The absence of characteristic lines in the range $30^\circ < 2\theta < 35^\circ$ leads to eliminate the presence of θ -, κ - and δ -alumina. As to titanium oxide, Raman spectroscopy and XRD clearly show the presence of rutile.

From the partial defection of aluminum in the tin concentration zone below alumina (Fig. 2m), a Sn-Ti phase is expected. A wide shoulder at about

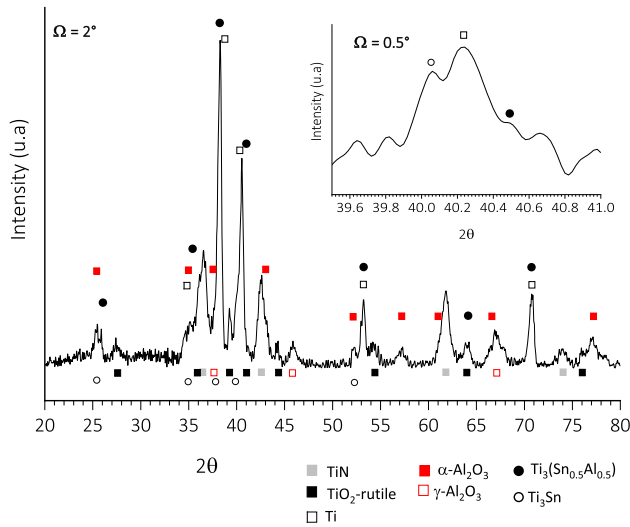


Figure 4 Grazing (2°) incidence 2θ X-ray diffraction pattern for DMAI500 after thermal oxidizing treatment at $600\text{ }^\circ\text{C}$ for 5000 h. Insert: Zoom at the $39\text{--}41^\circ$ region probed at 0.5° incidence angle.

$2\theta = 40.0^\circ$ on the low angle side of Ti (101) reflection argues for Ti_3Sn . The strongest reflection of Ti_3Sn is the (201) one at $2\theta = 40.00^\circ$.¹ Operating the diffractometer with $\omega = 0.5^\circ$ enhances the contribution of the Ti–Sn phase thus allowing to solve the shoulder and to measure $2\theta = 40.06^\circ$ for the Ti–Sn phase reflection and $2\theta = 40.22^\circ$ for the Ti (101) reflection. To our knowledge, no other Ti–Sn phase than Ti_3Sn has a strong reflection at about $2\theta = 40.0^\circ$.

The most intense peaks come from alpha-Ti, TiN, and $\text{Ti}_3(\text{Al}_{0.5}\text{Sn}_{0.5})$. The formula $\text{Ti}_3(\text{Al}_{0.5}\text{Sn}_{0.5})$ results from the measured positions of the diffraction peaks, assuming that Vegard’s law applies over the whole range $0 \leq x \leq 1$ for the solid solution $\text{Ti}_3(\text{Al}_x\text{Sn}_{1-x})$ (the unit-cell constants used for Ti_3Sn ($a = 0.4756\text{ pm}$, $c = 0.5911\text{ pm}$) and Ti_3Al ($a = 0.5751\text{ pm}$, $c = 0.4655\text{ pm}$) were taken from materials project.org¹. The presence of $\text{Ti}_3(\text{Al}_{0.5}\text{Sn}_{0.5})$ and Ti_3Sn accounts for the accumulation of Sn in the initial $\text{Al}_2\text{O}_3/\text{Ti6242S}$ interface (Fig. 3). A close examination of Fig. 3l–n shows that aluminum is only partially present in the Sn enriched Ti6242S upper zone, in agreement with the X-ray detection of both aluminum containing $\text{Ti}_3(\text{Al}_{0.5}\text{Sn}_{0.5})$ and aluminum defective Ti_3Sn phase.

Low incidence diffraction shows that the unit-cell of a part of the titanium is larger than in untreated

Ti6242S. For instance, with $\omega = 2^\circ$, the Ti strongest line (i.e., reflection (101)) is read at $2\theta = 40.32^\circ$ for untreated T6242S and at $2\theta = 40.38^\circ$ and $2\theta = 40.23^\circ$ for the treated coupon. The insert of Fig. 5 shows that with $\omega = 0.5^\circ$, only the line at $2\theta = 40.22^\circ$ is present. This fact signs some diffusion of oxygen in titanium near the interface. From the positions of lines (002) and (101), the resulting volume increase is 1.1%.

The intensity of $\text{Ti}_3(\text{Al}_{0.5}\text{Sn}_{0.5})$ reflections also are considerably reduced when recorded with $\omega = 0.5^\circ$: in the insert of Fig. 4, the weak shoulder at $2\theta = 40.5^\circ$ is the line (201) of $\text{Ti}_3(\text{Al}_{0.5}\text{Sn}_{0.5})$ which is the second more intense reflection, at $2\theta = 40.54^\circ$, when $\omega = 2^\circ$ is used. This is consistent with the observed lack of aluminum near the interface.

The presence of TiN and $\text{Ti}_3(\text{Al}_{0.5}\text{Sn}_{0.5})$ explains the Sn segregation below the oxide scale in Fig. 2i–o. The presence of a titanium nitrides (TiN or Ti_3N) layer below the oxide scale has already been observed after the oxidation of Ti6242S [35–37]. Atom probe tomography characterization of oxidized 6242S at $650\text{ }^\circ\text{C}$ in air for 1000 h revealed the presence of a layer of Ti-oxynitride and, below it, a layer of Ti_2N (with 35 at%N) enriched in Sn, Zr and Si and depleted in Al [37]. Therefore, it can be inferred that Al_2O_3 dissolution in the Ti-alloy leads to a less protective oxide layer, which allows inward nitrogen diffusion and formation of nitride below the oxide scale.

Figure 5 presents the evolution of the mass gain as a function of time for the bare and the DMAI500 coated Ti6242S coupons during oxidation in flowing dry synthetic air for a step-by-step increase in the temperature from 600 to $900\text{ }^\circ\text{C}$. The correspondence of annealing time with the stepwise increasing temperature is also reported. The coated coupon proves to be much more resistant than the uncoated one up to $800\text{ }^\circ\text{C}$, with a significant decrease in the conferred protection after a given time at $900\text{ }^\circ\text{C}$.

From these curves, considering that the oxidation kinetics follow a parabolic law, the parabolic rate constants k_p can be calculated according to:

$$k_p = \left[(\Delta m_f/S)^2 - (\Delta m_i/S)^2 \right] / (t_f - t_i) \quad (1)$$

where Δm_i and Δm_f are the mass gains of a sample with free surface S , at the beginning and at the end of each temperature dwell, respectively. This equation implies that the oxide layer formed at lower temperatures participates to the diffusion barrier [38]. The parabolic rate constants were determined at

¹ <https://materialsproject.org/materials/mp-1823/>, and <http://materialsproject.org/materials/mp-21030/> for Ti_3Al and Ti_3Sn , respectively. Last visited November 15, 2019.

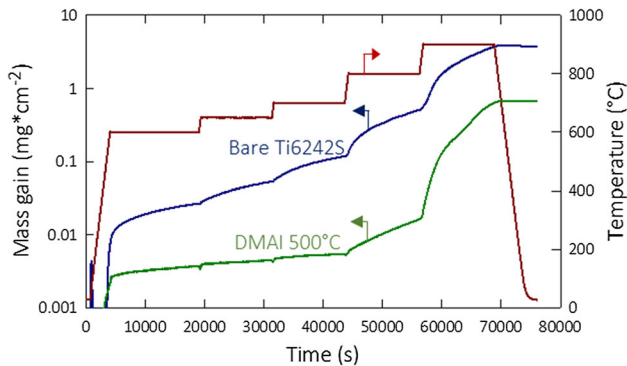


Figure 5 Mass gain per unit area of bare and DMAI500 coated Ti6242S alloy as a function of time, for stepwise increasing annealing temperature (red curve).

different operating temperatures for the four coatings DMAI300, DMAI500, DMAI700 and ATI520. The Arrhenius diagrams of Fig. 6 show them in comparison with the parabolic rate constants reported for three alumina allotropes, γ - Al_2O_3 , θ - Al_2O_3 , and α - Al_2O_3 on NiAl [39]. Clearly, the three coatings DMAI500, DMAI300 and ATI520 are highly efficient at providing oxidation protection during the short-term (10–20 h) thermogravimetric experiments between 600 and 700 °C. They are less efficient at 800 °C, except DMAI500, and become inefficient at higher temperatures. At 600–700 °C, the oxidation kinetics of our coated samples are similar to the oxidation kinetics obtained during γ - Al_2O_3 growth on NiAl. This is consistent with an oxygen uptake controlled by oxygen diffusion across the amorphous alumina coating.

This set of short-term TGA experiments was completed by long-term oxidation annealing in laboratory air at 600 °C, which is close to the maximum temperature of use of such alloys. The results are gathered in the diagram of Fig. 7, which presents the mass gain per unit area for bare and coated Ti6242S coupons as a function of the square root of annealing time for periods as long as 2000 h and 5000 h. Samples ATI520, DMAI300 and DMAI700 show mass gains of ca. 0.3 mg cm⁻² after 2300 h. For the same annealing time, two samples of the more efficient coating, DMAI500, show weight gains limited to ca. 0.180 mg cm⁻². In addition, this mass gain increases very slowly on extending the annealing time to 5000 h. In comparison, the mass gain of bare Ti6242S is 0.624, 1.143 and 1.633 mg cm⁻² after annealing for 1000, 2500 and 5010 h, respectively.

These results confirm the excellent oxidation protection conferred to Ti6242S by the 500-nm-thick amorphous Al_2O_3 films. The mass gain after 1000 h and 5000 h oxidation allows calculating the parabolic rate constant, using the relation:

$$k_p = (\Delta m/S)^2/t \quad (2)$$

The Arrhenius plot of Fig. 6 compiles results from short-term thermogravimetric tests and long-term isothermal tests. The parabolic rate constant increases with annealing time, consistently with a continuous degradation of the oxidation protection. However, despite this degradation, the parabolic rate constant for the DMAI500 sample is still two orders of magnitude lower than for the bare Ti6242S alloy. Such a result at a temperature typical of the highest operating temperatures of this alloy and for an annealing time as long as 5000 h is groundbreaking. Indeed, a decrease in two orders of magnitude of k_p should correspond to an increase in two orders of magnitude of the lifetime of the part.

Since most applications are running under thermal cycling, it is necessary to evaluate the behavior of the coated coupons under representative thermal cycling conditions. In such conditions, damage may rapidly occur, namely spallation of the ceramic coating on the metallic substrate, resulting in limited durability of the material. Eighty, one-hour cycles were performed between 50 and 600 °C, under flowing synthetic air in the thermobalance. Figure 8 presents the evolution of the mass gain per unit area for the DMAI300 sample and the temperature cycling variation as a function of time. The insert is a zoom on two cycles, detailing the temperature profile. The mass of the sample did not change at the microgram scale. Despite the rather short duration of this test compared with the usual service periods in turbine applications, it is a valuable indicator of the excellent adherence of the alumina layer on the alloy and of the relatively low level of elastic strain energy in the system during thermal cycling.

Figure 9 shows the hardness (H) depth profile from top surface to the substrate as a function of penetration depth, for the bare Ti6242S and for the DMAI500 sample after annealing at 600 °C for 5000 h. For the bare alloy, H increases from the bulk to the surface. It reaches a peak value of 11.5 GPa at 10 μm beneath the surface. Comparatively, the hardness of the alumina-coated alloy shows a very limited increase, thus demonstrating the efficient

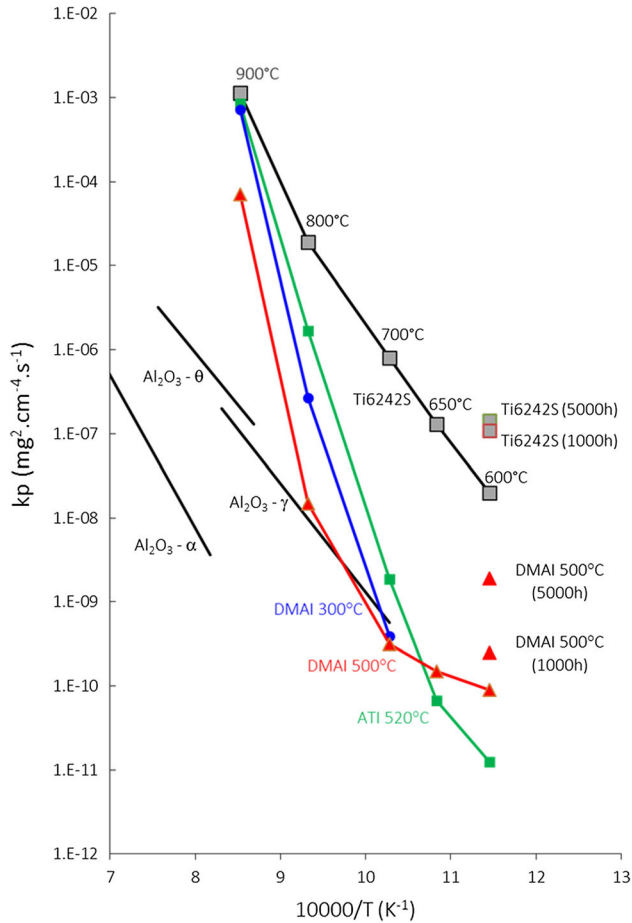


Figure 6 Parabolic rate constants from the short-term (10–20 h) oxidation experiments of the Ti6242S alloy, bare and coated with amorphous alumina processed from DMAI at 300 °C (DMAI300) and at 500 °C (DMAI500), and from ATI at 520 °C (ATI520). Data for long period, namely 1000 h and 5000 h, oxidation tests at 600 °C of bare and (DMAI500) coated Ti6242S are also reported. Results are compared with the kinetics of the development of gamma, theta and alpha alumina on NiAl, from [39].

protection conferred by the amorphous Al₂O₃ film against oxygen diffusion in the bulk alloy. Both coupons present similar hardness values of about 4.5–5.0 GPa beyond 60 μm penetration depth, slowly decreasing down to 4.0 GPa at ca. 200 μm below the surface.

Discussion

The behavior of the reported sample prepared from ATI at 480 °C compares with the one of ATI520 prepared in close conditions in the present study. These results validate the efficiency of the barrier coating

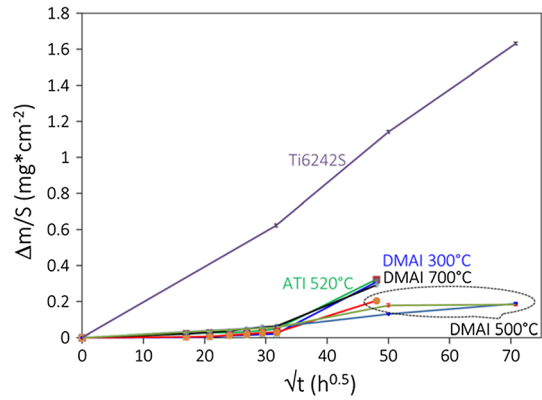


Figure 7 Mass gain per unit area for bare and coated Ti6242S coupons as a function of the square root of annealing time at 600 °C.

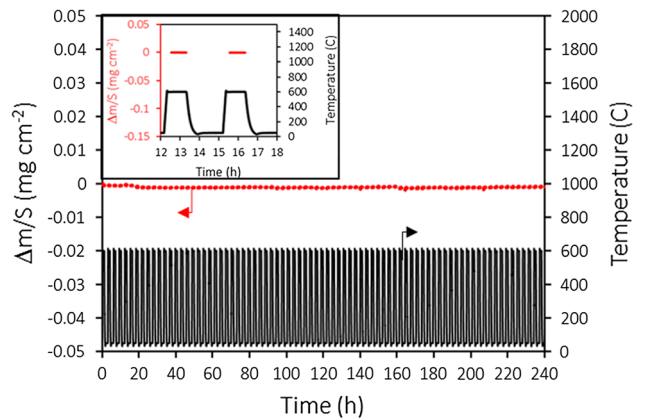
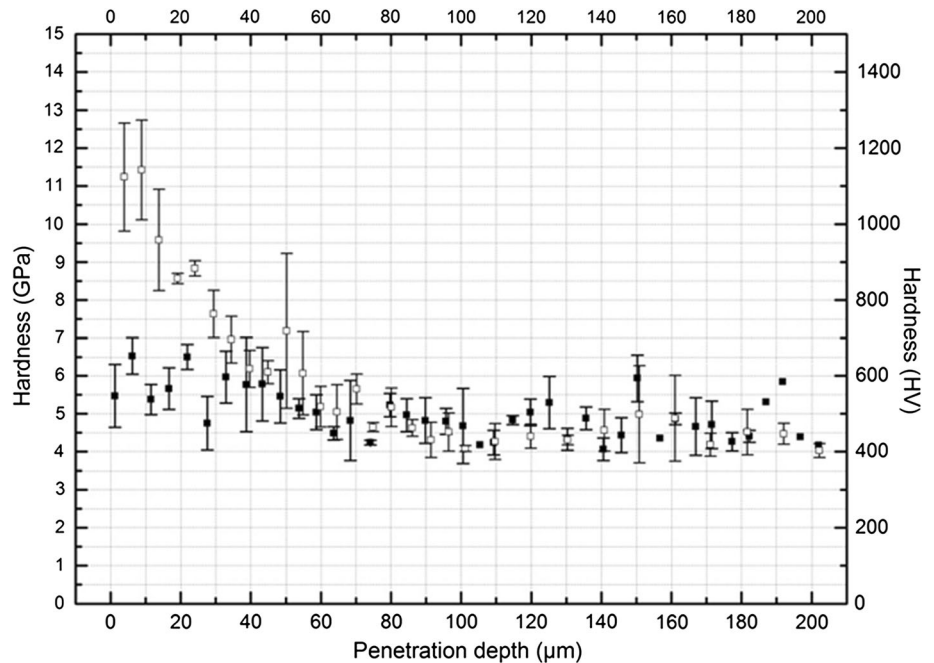


Figure 8 Evolution of the mass gain per unit area of the DMAI300 sample and of the temperature variation (cycling) as a function of time. The insert is a zoom on two cycles, detailing the temperature profile.

itself and explain the negligible oxygen intake of the alloy in its superficial zone underneath the coating. A large percentage of fivefold coordinated Al ions (⁵Al) distinctly hallmarks the structure of amorphous Al₂O₃ in comparison with the crystallized varieties that contain fourfold (⁴Al) and/or sixfold (⁶Al) coordinated ions only. A very high-field NMR study of amorphous Al₂O₃ grown from ATI showed that the respective percentages of ⁴Al, ⁵Al, and ⁶Al vary with deposition temperature [40]. Independently of the thickness between 200 and 1000 nm, films processed at ca. 500 °C present a maximum concentration of ⁴Al (54%) and ⁵Al (41%) sites and utmost structural disorder from NMR peaks analysis and chemical shift distributions. The most disordered structure is the less propitious to grain boundary formation, in which oxygen diffusion rates are the

Figure 9 Hardness depth profile as a function of penetration depth for the bare Ti6242S (empty squares) and for the DMAI500 coupon after annealing at 600 °C for 5000 h.



lowest and therefore creates the most efficient diffusion barrier. The deposition temperature of ca. 500 °C also corresponds to the highest film hardness (10.8 ± 0.8 GPa) and Young's modulus (155 ± 6 GPa) [23]. Films processed from DMAI also show variable respective percentages in ^{41}Al , ^{51}Al , and ^{61}Al ions with the deposition temperature, and utmost disorder around 500 °C [32].

Hardness profile is an illustration of the concentration profile of oxygen in Ti6242S [7, 33]. The embrittlement of the latter is due to the dissolution of oxygen therein. The limited mass gain shown in the thermogravimetric curves for the coated alloy corresponds to a negligible growth of TiO_2 and to the absence of dissolved oxygen in the metallic matrix. Indeed, the alpha phase of Ti can dissolve up to 33 at% oxygen. From 1000 ppm at most, oxygen hardens titanium, increases Young's modulus and decreases the ductility [7]. Wiesing et al. [41] performed a detailed XPS analysis of the oxidation of TiAlN alloy and reported similar results, namely a quasi-metallic character of subsurface oxygen, not affecting the $\text{Ti}2p$ lineshape.

The excellent resistance to thermal cycling of the $\text{Al}_2\text{O}_3/\text{Ti6242s}$ can be related to the limited amount of compressive stress in the alumina layer during cooling. Indeed, the planar stress in the alumina due to temperature variation equals:

$$\sigma_{\text{ox}} = \frac{-E_{\text{ox}} \Delta T (\alpha_{\text{M}} - \alpha_{\text{ox}})}{(1 - \nu) \left(1 + \frac{E_{\text{ox}} \epsilon_{\text{ox}}}{E_{\text{M}} \epsilon_{\text{M}}}\right)}$$

Which can be simplified, considering that the ceramic coating is very thin, as:

$$\sigma_{\text{ox}} = \frac{-E_{\text{ox}} \Delta T (\alpha_{\text{M}} - \alpha_{\text{ox}})}{(1 - \nu)}$$

The expansion coefficient of alloy Ti6242s is $\alpha_{\text{M}} = 7.7 \times 10^{-6} \text{ K}^{-1}$, and the one of alumina $\alpha_{\text{ox}} = 14.7 \times 10^{-6} \text{ K}^{-1}$. The highest hardness of 11.5 GPa measured for annealed bare Ti6242S alloy is in good agreement with the one of titanium oxide when the O/Ti ratio is from 1.8 to 2.0 [42], and therefore, the hardening effect is certainly due to the dissolution of oxygen within the diffusion zone. For both coupons, the hardness values decrease to 4.0 GPa at ca. 200 μm below the surface, slowly approaching the 3.6 GPa expected value of the bare Ti6242S alloy.

The mechanistic insight in the reported reactive diffusion phenomena is out of the scope of the work, which covers the entire process-structure-properties-performance relationship. However, these results should be a valuable input for such forthcoming dedicated studies. Overall, the obtained results confirm that such very thin amorphous alumina films meet the specifications for a long-term oxidation protection of Ti-based alloys. This high performance is due to the dense, highly disordered, grain

boundaries-free network meaning that the application domain is restricted up to ca. 650 °C, the temperature where initiation of the crystallization of the amorphous Al₂O₃ takes place. The Al₂O₃/Ti-alloy couple may not be thermodynamically stable, and this leads in the present conditions to the formation, among other phases, of α -Al₂O₃, and rutile at the interface between the film and the alloy, as expected. However, the kinetics of the reaction with the Ti-alloy in the investigated conditions are extremely slow and they pertain even in the most severe case; i.e., at 600 °C up to 5000 h, despite the submicrometric thickness of the Al₂O₃ film. This result combined with the intrinsic ability of gas phase chemical deposition processes (MOCVD and also atomic layer deposition, ALD) to conformally coat non-line-of-sight surfaces shows promise for their use in complex parts such as turbine blades, including their millimetric size cooling features.

Conclusions

The aim of this work is to tackle the intrinsic weakness of limited resistance to high-temperature oxidation of titanium alloys. We apply well-established MOCVD processes to yield dense, amorphous Al₂O₃ coatings on the Ti6242S alloy. Numerous oxidation tests reveal, in a coherent way, a significant improvement of its oxidation resistance. First, the parabolic rate constants of the mass gain of the coated Ti6242S coupons are reduced up to two orders of magnitude compared with the bare material in short-term isothermal oxidation conditions. Then, 5000 h long oxidation of the coated alloy results in 0.180 mg cm⁻² weight gain to be compared with 1.143 mg cm⁻² for the bare alloy. In addition, the hardness profiles determined by nanoindentation on cross sections of oxidized coupons reveal a very limited oxygen dissolution in subsurface regions, for the coated alloy. Finally, cyclic oxidation tests consisting of eighty, 1 h cycles between 50 and 600 °C, which reproduce in operando conditions for this material, show null mass gain for the coated sample and consequently they illustrate the durability of the efficient oxidation barrier property of the amorphous Al₂O₃ coatings. We show that in harsh oxidation environment, an interfacial layer is formed between the alumina coating and the Ti-alloy, containing the Sn-rich Ti₃(Al_{0.5}Sn_{0.5}) phase. These results

demonstrate that MOCVD processed very thin Al₂O₃ films on Ti remain stable in operando over a very long period and present an efficient solution to the limited high-temperature oxidation resistance of Ti-alloys in general. They may be used in key enabling technologies where mass gain for energy savings and environmental protection is required.

Acknowledgements

The support by the STAE-RTRA Foundation (Toulouse, France) under the RTRA-STAE/2014/P/VIMA/12 (Fondation Sciences et Technologies pour l'Aéronautique et l'Espace) Project Grant is acknowledged.

Authors' contribution

DS and LB performed the deposition experiments and the SEM characterizations. They contributed equally to this work. RL and VT performed the mechanical characterizations. TD performed the nanoAuger characterizations. ANG performed the XRD characterizations. DM defined the experimental design for isothermal and cyclic oxidation tests. CV designed the project and coordinated the work. All co-authors contributed to the manuscript composition.

Compliance with ethical standards

Conflict of interest The authors declare that they have no conflict of interest.

References

- [1] Lütjering G, Williams JC (2007) Titanium. Springer, Berlin
- [2] Shenoy RN, Unnam J, Clark RK (1986) Oxidation and embrittlement of Ti-6Al-2Sn-4Zr-2Mo alloy. *Oxid Met* 26:105–124
- [3] Leyens C, Peters M (2003) Titanium and titanium alloys: fundamentals and applications. Wiley-VCH Verlag GmbH & Co. KGaA, Weinheim
- [4] Kakehi K, Hashimoto T (2008) Influence of oxidation on mechanical properties of the heat-resistant titanium alloy DAT54. *J Jpn Inst Met* 72:819–824
- [5] Pilchak AL, Porter WJ, John R (2012) Room temperature fracture processes of a near-alpha titanium alloy following

- elevated temperature exposure. *J Mater Sci* 47:7235–7253. <https://doi.org/10.1007/s10853-012-6673-y>
- [6] Gurappa I (2003) Prediction of titanium alloy component life by developing an oxidation model. *J Mater Sci Lett* 22:771–774. <https://doi.org/10.1023/A:1023784800315>
- [7] McReynolds KS, Tamirisakandala S (2011) A study on alpha-case depth in Ti-6Al-2Sn-4Zr-2Mo. *Metall Mater Trans A* 42A:1732–1736
- [8] Xiao WL, Murakami H, Ping DH, Yamabe-Mitarai Y (2013) Microstructure and oxidation behaviors of near-alpha Ti-6.5Al-4Sn-4Zr-0.5Mo-based alloys with Ir addition. *J Mater Sci* 48:3363–3369. <https://doi.org/10.1007/s10853-012-7118-3>
- [9] Rong J, Wang Y, Li RY, Yu XH, Meng K (2018) Interface structure between titanium substrate and high temperature oxidation resistant aluminum-base coatings. *Rare Met Mater Eng* 47:682–686
- [10] Shen ZJ, Zhang YN, Yu XH (2019) Interfacial microstructure evolution mechanism of high temperature oxidation-resistant Al-based coating on Ti alloy surface. *Mater Res Express* 6:086472
- [11] Bobzin K, Brogelmann T, Kalscheuer C, Liang T (2017) High temperature oxidation protection of gamma-titanium aluminide using (Cr, Al) ON coatings deposited by high-speed physical vapor deposition. *Surf Coat Technol* 332:2–11
- [12] Li WB, Chen MH, Wang C, Zhu SL, Wang FH (2013) Preparation and oxidation behavior of SiO₂-Al₂O₃-glass composite coating on Ti-47Al-2Cr-2Nb alloy. *Surf Coat Technol* 218:30–38
- [13] Zhang XJ, Gao YH, Ren BY, Tsubaki N (2010) Improvement of high-temperature oxidation resistance of titanium-based alloy by sol-gel method. *J Mater Sci* 45:1622–1628. <https://doi.org/10.1007/s10853-009-4138-8>
- [14] Sarkar S, Datta S, Das S, Basu D (2009) Oxidation protection of gamma-titanium aluminide using glass-ceramic coatings. *Surf Coat Technol* 203:1797–1805
- [15] Ru Q, Hu SJ (2010) Effects of Ti_{0.5}Al_{0.5}N coatings on the protecting against oxidation for titanium alloys. *Rare Met* 29:154–161
- [16] Delmas M, Poquillon D, Kihn Y, Vahlas C (2005) Al-Pt MOCVD coatings for the protection of Ti6242 alloy against oxidation at elevated temperature. *Surf Coat Technol* 200:1413–1417
- [17] Delmas M, Ucar M, Ressler L, Pons M, Vahlas C (2004) MOCVD processed platinum aluminide coatings on titanium alloys. *Surf Coat Technol* 188:49–54
- [18] Delmas M, Vahlas C (2007) Microstructure of metalorganic chemical vapor deposited aluminium coatings on Ti6242 alloy. *J Electrochem Soc* 154:D538–D542
- [19] Thomann A-L, Vahlas C, Aloui L, Samélor D, Caillard A, Shaharil N, Blanc R, Millon E (2011) Conformity of aluminum thin films deposited onto micro-patterned silicon wafers by pulsed laser deposition, magnetron sputtering, and CVD. *Chem Vap Depos* 17:366–374
- [20] Jiang ZP, Yang X, Liang YF, Hao GJ, Zhang H, Lin JP (2018) Favorable deposition of gamma-Al₂O₃ coatings by cathode plasma electrolysis for high-temperature application of Ti-45Al-8.5Nb alloys. *Surf Coat Technol* 333:187–194
- [21] Wang QM, Renteria AF, Schroeter O, Mykhaylonka R, Leyens C, Garkas W, Baben MT (2010) Fabrication and oxidation behavior of Cr₂AlC coating on Ti6242 alloy. *Surf Coat Technol* 204:2343–2352
- [22] Riviere JP, Pichon L, Drouet M, Poquillon D, Galdikas A (2007) Silicon based coatings deposited by dynamic ion mixing for oxidation protection of a Ti6242 alloy. *Surf Coat Technol* 201:8343–8347
- [23] Balcaen Y, Radutoiu N, Alexis J, Béguin JD, Lacroix L, Samélor D, Vahlas C (2011) Mechanical and barrier properties of MOCVD processed alumina coatings on TA6V titanium alloy. *Surf Coat Technol* 206:1684–1690
- [24] Boisier G, Raciulete M, Samélor D, Pébère N, Gleizes AN, Vahlas C (2008) Electrochemical behavior of chemical vapor deposited protective aluminium oxide coatings on Ti6242 titanium alloy. *Electrochem Sol State Lett* 11:C55–C57
- [25] Samélor D, Baggetto L, Laloo R, Turq V, Duguet T, Monceau D, Vahlas C (2010) Amorphous alumina films efficiently protect Ti6242S against oxidation and allow operation above 600 °C. In: Shabadi R, Ionescu M, Jeandin M, Richard C, Chandra T (eds) *Thermec 2018: 10th international conference on processing and manufacturing of advanced materials*, pp 1846–1852
- [26] Baggetto L, Esvan J, Charvillat C, Samélor D, Vergnes H, Caussat B, Gleizes A, Vahlas C (2015) Alumina thin films prepared by direct liquid injection chemical vapor deposition of dimethylaluminum isopropoxide: a process-structure investigation. *Phys Status Solidi C* 12:989–995
- [27] Samélor D, Sovar MM, Stefanescu A, Gleizes AN, Alphonse P, Vahlas C (2005) Low temperature CVD route for the preparation of alumina coatings with high specific surface area. In: Devi A, Fischer R, Parala H, Allendorf MD, Hitchman ML (eds) *15th European conference on chemical vapor deposition*, pp 1051–1058
- [28] Baggetto L, Charvillat C, Esvan J, Thébault Y, Samélor D, Vergnes H, Caussat B, Gleizes A, Vahlas C (2015) A process-structure investigation of aluminum oxide and oxycarbide thin films prepared by direct liquid injection chemical vapor deposition of dimethylaluminum isopropoxide (DMAI). *Chem Vap Depos* 21:343–351

- [29] Monceau D, Poquillon D (2004) Continuous thermogravimetry under cyclic conditions. *Oxid Met* 61:143–163
- [30] Oliver WC, Pharr GM (1992) An improved technique for determining hardness and elastic-modulus using load and displacement sensing indentation experiments. *J Mater Res* 7:1564–1583. <https://doi.org/10.1557/JMR.1992.1564>
- [31] Gleizes A, Vahlas C, Sovar MM, Samélor D, Lafont MC (2007) CVD-fabricated aluminum oxide coatings from aluminum tri-iso-propoxide: correlation between processing conditions and composition. *Chem Vap Depos* 13:23–29
- [32] Baggetto L, Sarou-Kanian V, Florian P, Gleizes AN, Massiot D, Vahlas C (2017) Atomic scale structure of amorphous aluminum oxyhydroxide, oxide and oxycarbide films probed by very high field ^{27}Al nuclear magnetic resonance. *Phys Chem Chem Phys* 19:8101–8110
- [33] Dupressoire C, Rouaix-Vande Put A, Emile P, Archambeau-Mirguet C, Peraldi R, Monceau D (2017) Effect of nitrogen on the kinetics of oxide scale growth and of oxygen dissolution in the Ti6242S titanium-based alloy. *Oxid Met Xia* 87:343–353
- [34] Rakowski J, Monceau D, Pettit FS, Meier GH (1993) The oxidation and embrittlement of α_2 (Ti₃Al) titanium aluminides. In: Newcomb SB, Bennett MJ (eds) *Microscopy of oxidation-2*. Selwyn College, University of Cambridge, The Institute of Materials, London, pp 476–487
- [35] Kanjer A, Optasanu V, de Lucas MCM, Heintz O, Geoffroy N, Francois M, Berger P, Montesin T, Lavis L (2018) Improving the high temperature oxidation resistance of pure titanium by shot-peening treatments. *Surf Coat Technol* 343:93–100
- [36] Abdallah I, Dupressoire C, Laffont L, Monceau D, Put AV (2019) STEM-EELS identification of TiOXNY, TiN, Ti₂N and O, N dissolution in the Ti₂642S alloy oxidized in synthetic air at 650 degrees C. *Corros Sci* 153:191–199
- [37] Dupressoire C, Descoins M, Vande Put A, Mangelinck D, Emile P, Monceau D (2019) The nitrogen effect on the oxidation behaviour of Ti₆242S titanium-based alloy: contribution of atom probe tomography. In: 14th world conference on titanium, EdP Science, Nantes (in press)
- [38] Monceau D, Pieraggi B (1998) Determination of parabolic rate constants from a local analysis of mass-gain curves. *Oxid Met* 50:477–493
- [39] Brumm MW, Grabke HJ (1992) The oxidation behaviour of NiAl-I phase transformations in the alumina scale during oxidation of NiAl and NiAl-Cr alloys. *Corros Sci* 33:1677–1690
- [40] Sarou-Kanian V, Gleizes AN, Florian P, Samélor D, Massiot D, Vahlas C (2013) Temperature-dependent 4-, 5- and 6-fold coordination of aluminum in MOCVD-grown amorphous alumina films: a very high field Al- ^{27}Al -NMR study. *J Phys Chem C* 117:21965–21971
- [41] Wiesing M, de los Arcos T, Grundmeier G (2017) The Thermal oxidation of TiAlN high power pulsed magnetron sputtering hard coatings as revealed by combined ion and electron spectroscopy. *Adv Mater Interfaces* 4:1600861
- [42] Xia J, Li CX, Dong H, Bell T (2006) Nanoindentation and nanoscratch properties of a thermal oxidation treated gamma-TiAl based alloy. *Surf Coat Technol* 200:4755–4762

Publisher's Note Springer Nature remains neutral with regard to jurisdictional claims in published maps and institutional affiliations.